

1 **Influence of the High Arctic Igneous Province on the Cenomanian/Turonian Boundary**
2 **Interval, Sverdrup Basin, High Canadian Arctic**

3

4 Claudia J. Schröder-Adams¹, Jens O. Herrle², David Selby^{3,4}, Alex Quesnel¹, Gregory Froude¹

5

6 ¹Department of Earth Sciences, Carleton University, Ottawa, Ontario, K1S 5B6, Canada

7 ²Institute of Geosciences, Altenhoferallee 1, Goethe-University Frankfurt, Biodiversity and
8 Climate Research Centre (BIK-F), D-60438 Frankfurt am Main, Germany

9 ³Department of Earth Sciences, Durham University, DH1 3LE, Durham, United Kingdom

10 ⁴State Key Laboratory of Geological Processes and Mineral Resources, School of Earth
11 Resources, China University of Geosciences Wuhan, Wuhan, China

12

13 Corresponding author: Claudia.schroderadams@carleton.ca

14

15 Keywords: Cenomanian/Turonian Boundary Interval, High Arctic Large Igneous Province,

16 ¹⁸⁷Os/¹⁸⁸Os isotope composition, Carbon isotopes, Arctic Sverdrup Basin, Foraminifera

17

18

19 **Abstract**

20 Emplacement of Large Igneous Provinces (LIPs) had a major effect on global climate,
21 ocean chemistries as traced in sedimentary records and biotic turnovers. The linkage between
22 LIPs and oceanic anoxic events has been documented with the Cenomanian/Turonian boundary
23 event and Oceanic Anoxic Event 2 (OAE2). The Caribbean LIP and High Arctic Large Igneous
24 Province (HALIP) are regarded as possible triggers. The pericratonic Arctic Sverdrup Basin is
25 the partial location of the HALIP, where little is known about sedimentary, geochemical and
26 biotic responses to the HALIP phases. Sedimentary strata at Glacier Fiord, Axel Heiberg Island,
27 exhibit a dynamic Cretaceous polar carbon burial history within the lower to middle Cenomanian
28 Bastion Ridge Formation and upper Cenomanian to Turonian part of the Kanguk Formation. We
29 present the first initial $^{187}\text{Os}/^{188}\text{Os}$ (Os_i) composition profile for a polar Cenomanian/Turonian
30 boundary interval (~100-93.9 Ma) linked to recently dated magmatic phases of the Strand Fiord
31 Formation, part of the HALIP. The carbon isotope record coupled with the Os_i profile show two
32 events in the upper Cenomanian interval marked by positive carbon perturbations and shifts to
33 more non-radiogenic Os_i compositions. The earlier short-lived event is interpreted as result of
34 weathering of the surrounding Strand Fiord volcanics causing a local non-radiogenic Os_i signal.
35 Coinciding transgressive shorelines led to an increase in marine and terrestrially derived organic
36 matter. Subsequently, injection of mantle-derived basalts into organic rich sediments is credited
37 with causing the release of methane documented in a distinct negative carbon isotope excursion.
38 We speculate that the methane release of the HALIP was an important contribution for rapid
39 global warming caused by increasing atmospheric CO_2 levels associated with the OAE2 event
40 likewise recognized in the Sverdrup Basin. As climate cooled in the middle and late Turonian,
41 carbon burial decreased under increasingly oxygenated benthic conditions. Epifaunal

42 foraminiferal species, adapted to low oxygen conditions, persisted during the OAE2. Our
43 Cenomanian to Turonian multiproxy record of the Sverdrup Basin distinguishes between local
44 and global signals within a restricted High Arctic basin. Our results demonstrate the interplay
45 between basin tectonism and sea-level change, increased weathering during transgressive phases,
46 seafloor processes such as hydrothermal activity and methane release and biotic response to a
47 complex paleoceanography. With future reliable dated frameworks this unique polar record will
48 facilitate correlations to other polar basins and records of lower paleolatitudes.

49 **1. Introduction**

50 The influence of Large Igneous Provinces (LIPs) on paleoclimate, ocean chemistries and
51 paleoecosystems has become increasingly apparent (e.g., Erba et al. 2015; Ernst and Youbi,
52 2017). The contribution of these large magmatic events to global greenhouse climate phases is
53 demonstrated at the Cenomanian/Turonian boundary event and the global Oceanic Anoxic Event
54 2 (OAE2) where the Caribbean Large Igneous Province (CLIP) is considered as the main
55 causative driver (Snow et al., 2005; Holmden et al., 2016; Scaife et al., 2017). Although the High
56 Arctic LIP (HALIP) is largely understudied it is also considered to be a driving mechanism of
57 OAE2 (Tegner et al., 2011; Zheng et al., 2013). More recently, a chronological linkage between
58 the LIP emplacement and the global carbon burial event is demonstrated with osmium isotope
59 records (Turgeon and Creaser, 2008; Du Vivier et al., 2014; 2015).

60 Documentation of OAE2 in the Sverdrup Basin, a pericratonic basin located in the High
61 Arctic Canadian Archipelago, is relatively new (Pugh et al., 2014; Lenniger et al., 2014; Herrle
62 et al., 2015). The feedback mechanism between LIP emplacement and the Arctic
63 Cenomanian/Turonian boundary event as recorded in the Arctic has not been investigated. In this
64 respect the Sverdrup Basin is a promising site since it partially records the HALIP, where several

65 phases of magmatic activity can be distinguished (Tegner et al., 2011; Estrada and Henjes-Kunst,
66 2013, 2016; Jowitt et al., 2014; Saumur et al., 2016).

67 Glacier Fiord on Axel Heiberg Island in the Canadian High Arctic (Figs. 1A, B) provides
68 a unique site, where Cenomanian/Turonian strata are well exposed in outcrop with a documented
69 OAE2 interval (Schröder-Adams et al., 2014; Herrle et al., 2015). Furthermore, this site is near
70 (~50 km) to the Strand Fiord Formation containing flood basalts (Fig. 1B) that are part of the
71 younger HALIP phases ranging from 105 to 92 Ma (Villeneuve and Williamson, 2006; Estrada
72 et al., 2016). The Strand Fiord volcanics are extensively exposed in the southern region of Axel
73 Heiberg Island (Fig. 1B). Thus, this location offers a favourable geological setting to investigate
74 the direct influence of a magmatic event that is part of a major LIP on geochemical cycling and
75 marine ecosystems. To link the eruption of the Strand Fiord volcanics to polar and global
76 paleoceanographic and paleoecosystem changes we apply carbon isotopes coupled with the first
77 osmium isotope record ($^{187}\text{Os}/^{188}\text{Os}$) from the Cretaceous Sverdrup Basin, and selected whole
78 rock geochemistry and Rock Eval analysis. Benthic redox conditions are corroborated with
79 benthic foraminiferal abundances and morphotype distribution and paleoenvironmental
80 interpretations are aided by palynomorph occurrences. Integration of these data allow us to: a)
81 explore Cenomanian to Turonian carbon burial histories and geochemical changes within a polar
82 basin; b) document linkages to the HALIP and ultimately the rifting history of the Amerasia
83 Basin; and c) distinguish local from global paleoenvironmental controls on the Sverdrup Basin.

84 **2. Geological Setting**

85 *2.1. The Cenomanian/Turonian boundary interval in the Sverdrup Basin*

86 The Cenomanian/Turonian boundary lies within the lower Kanguk Formation, a mudrock
87 dominated transgressive unit spanning the upper Cenomanian to Campanian in the Sverdrup

88 Basin (Embry and Beauchamp, 2008). Currently, three localities are described from the
89 Canadian High Arctic where the Cenomanian/Turonian boundary interval with a pronounced
90 positive $\delta^{13}\text{C}_{\text{org}}$ signal is reported. At Hoodoo Dome on Ellef Ringnes Island (Fig. 1A),
91 representing a central basin position, OAE2 occurs within a silty shale at the base of the Kanguk
92 Formation immediately overlying the deltaic sandstones of the Hassel Formation (Fig. 2) (Pugh
93 et al., 2014). At May Point (east central Axel Heiberg Island, Fig. 1B), positioned closer to the
94 eastern margin of the Sverdrup Basin, the OAE2 interval is characterized by ‘paper shale’ at the
95 base of the Kanguk Formation (Lenniger et al., 2014). At Glacier Fiord (southern Axel Heiberg
96 Island, Fig. 1B) with a similar basin position to May Point, the OAE2 interval is documented in a
97 ‘paper shale’ within the lower Kanguk Formation (Herrle et al., 2015). At Glacier Fiord the
98 Kanguk Formation overlies the Bastion Ridge Formation (Figs. 2, 3A), that in turn overlies the
99 Hassel Formation (MacRae, et al., 1996; Schröder-Adams et al., 2014). The silty shale unit of the
100 Bastion Ridge Formation is interpreted to record deposition in a regionally restricted basin
101 (MacRae, 1992). In vicinity to Strand Fiord (Fig. 2) the Bastion Ridge Formation lies between
102 the Hassel Formation and the Strand Fiord volcanics or is interbedded with the volcanics
103 (Ricketts et al., 1985; MacRae et al., 1996); at Glacier Fiord, where no volcanics were deposited,
104 the Bastion Ridge Formation separates the Hassel from the Kanguk Formation (Fig. 3A)
105 (Schröder-Adams et al., 2014).

106 Benthic foraminifera at Glacier Fiord have been used to pinpoint the Albian/Cenomanian
107 and Cenomanian/Turonian boundaries (Schröder-Adams et al., 2014). Carbon isotope records
108 have clearly identified the position of the OAE2 interval (Herrle et al., 2015). In addition, several
109 CA-ID-TIMS weighted $^{206}\text{Pb}/^{238}\text{U}$ zircon dates of bentonites (Fig. 4) including one from the
110 Bastion Ridge Formation and five from the Turonian part of the Kanguk Formation above OAE2

111 have been determined (Davis et al., 2016). The bentonite in the middle of the Bastion Ridge
112 Formation yielded a weighted $^{206}\text{Pb}/^{238}\text{U}$ zircon age of 98.3 ± 1.8 Ma, suggesting a maximum
113 age for the sampled horizon. The stratigraphically oldest bentonite of the Turonian bentonite
114 swarm within the Kanguk Formation yielded a weighted $^{206}\text{Pb}/^{238}\text{U}$ zircon age of 93.03 ± 0.21
115 Ma. Coupling this age with the top of the positive carbon isotope excursion closely placed to the
116 Cenomanian/Turonian boundary at 93.9 Ma a sedimentation rate of 19 m Ma^{-1} is calculated for
117 the lower Turonian (Davis, et al., 2016).

118 *2.2. The HALIP and Strand Fiord Formation*

119 Volcanic and intrusive rocks of the HALIP are exposed in the Arctic region with large
120 volumes being mapped within the Sverdrup Basin on Ellef and Amund Ringnes, Axel Heiberg
121 and Ellesmere islands (e.g. Embry and Osadetz, 1988; Ricketts et al., 1985; Estrada and Henjes-
122 Kunst, 2004, 2013; Buchan and Ernst, 2006; Evenchick et al., 2015). Two dominant pulses are
123 recognized, an older phase dominated by tholeiitic magmas spanning approximately 130 to ~83
124 Ma ago and a younger alkaline phase from 93 to 60 Ma (Embry and Osadetz, 1988; Tegner et al,
125 2011; Thorarinsson et al., 2011; Estrada et al., 2016). Of interest here is the last pulse of the
126 older phase associated with the volcanics of the Strand Fiord Formation.

127 The continental flood basalts of the Strand Fiord Formation (Souther, 1963;
128 Thorsteinsson, 1971; Ricketts et al., 1985) are exposed on the Kanguk Peninsula of Axel Heiberg
129 Island (Fig. 1B) where they reach a maximum thickness of ~950 m at Bunde Fiord (Williamson
130 et al., 2016), and thin towards the east and south (Ricketts et al, 1985; MacRae et al., 1996). At
131 Bunde Fiord subaerial lavas dominate, whereas at Strand Fiord lavas either overly or interfinger
132 with marine shales of the Bastion Ridge Formation. At Strand Fiord volcanic extrusion was
133 initially submarine and rapid build-up changed to a subaerial deposition. The Strand Fiord

134 Formation consists of tholeiitic icelandite flows (Pahoehoe and aa flows) with minor occurrences
135 of epiclastic and pyroclastic components that increase towards the east and south with evidence
136 of laharic flows reaching the marine basin. The thickness of individual flows ranges from 6 to 60
137 m (Ricketts et al., 1985). The Strand Fiord Formation is not present at the head of Glacier Fiord
138 (Figs. 1B, 2).

139 Stratigraphically, the Strand Fiord volcanics overly the upper Albian to Cenomanian
140 Hassel Formation (Figs. 2, 3B). No siliciclastic material of Hassel origin was found in the Strand
141 Fiord volcanics (Ricketts et al., 1985). The volcanics overlie and partly interfinger with the time-
142 equivalent Cenomanian Bastion Ridge Formation confirmed by injection structures at their
143 contacts and the presence of bombs and lapilli-sized volcanic clasts within the upper Bastion
144 Ridge Formation (Ricketts et al., 1985). The marine shales of the Kanguk Formation top the
145 volcanics (Figs. 2, 3D; Ricketts et al., 1985; MacRae et al., 1996). Detailed mapping at Strand
146 Fiord characterized two different eruption phases of the Strand Fiord volcanics (Ricketts et al.,
147 1985; Williamson, 1988). Based on palynology of interlayered sedimentary strata a late Albian
148 to early Cenomanian age was originally suggested for the Strand Fiord Formation (Ricketts et al.,
149 1985; Embry and Osadetz, 1988; Nuñez- Betelu et al., 1994; MacRae et al., 1996) which
150 represents an early precursor phase close to the Albian/Cenomanian boundary. A whole rock
151 basalt $^{40}\text{Ar}/^{39}\text{Ar}$ age of 95.3 ± 0.2 Ma from the uppermost lava flow at Strand Fiord (Fig. 1B)
152 constrains the later phase into the late Cenomanian (Tarduno et al., 1998). Furthermore, two
153 separate feeder dykes related to the late Strand Fiord HALIP pulse close to South Fiord on Axel
154 Heiberg Island (Fig. 1B) delivered U-Pb CA-ID-TIMS $^{206}\text{Pb}/^{238}\text{U}$ zircon weighted average ages
155 of 95.18 ± 0.35 Ma and 95.41 ± 0.12 Ma (Kingsbury et al., 2018). The emplacement/eruption
156 duration of the late phase is considered to be < 1 myr (Kingsbury et al., 2018). These late

157 Cenomanian ages correlate well with age estimates derived from foraminiferal biostratigraphy
158 and carbon isotope stratigraphy (Schröder-Adams et al., 2014; Herrle et al., 2015) and a
159 bentonite age of $<98.3 \pm 1.8$ Ma (Davis et al., 2016) of the Bastion Ridge Formation at Glacier
160 Fiord.

161 *2.3. Cenomanian/Turonian lithology at Glacier Fiord*

162 The Glacier Fiord section (N 78° 37.795', W 89° 53.682', Fig. 1B) discussed here covers
163 112 m that forms the entire Bastion Ridge Formation and 133 m of the overlying lower Kanguk
164 Formation. The Bastion Ridge Formation overlies a thin paleosol at the top of the Hassel
165 Formation, which represents the widespread Albian/Cenomanian disconformity (Embry and
166 Dixon, 1990; Schröder-Adams et al., 2014). The 112 m thick Bastion Ridge Formation consists
167 of a 70 m thick dark grey to black to rusty oxidized silty shale (Fig. 3C), containing very fine-
168 grained sandstone beds and siderite concretions and a 15 cm thick bentonite at 50 m. This
169 interval is followed by a 10 m thick bioturbated sandstone that contains a lower 6 m thick yellow
170 to brown unit and a 4 m thick upper grey unit (Fig. 3C). This is followed by a 7 m thick covered
171 interval overlain by 25 m of silty mudrock with several distinct siderite beds (Fig. 4) interpreted
172 as freshwater siderites (Ross et al., in press), which suggests a possible hiatus in the middle
173 Cenomanian (Fig. 4). At 112 m the lithology changes abruptly to dark grey 'paper shale'
174 marking the base of the transgressive Kanguk Formation. The nearly 500 m thick formation
175 (Schröder-Adams et al., 2014) of which the lower 135 m are discussed here are interbedded with
176 frequent bentonites.

177 Geochemical and isotope data and details of section correlation, materials and analytical
178 methodologies are presented in the Supplementary Materials.

179 3. Results

180 3.1. Carbon and Osmium Isotope Stratigraphy

181 The existing $\delta^{13}\text{C}_{\text{org}}$ stratigraphy of the Glacier Fiord locality (Herrle et al., 2015) is
182 further refined here with additional data points (Fig. 4, Table 2) from 85 m to 132 m to improve
183 the resolution within the Cenomanian/Turonian boundary interval. The lower to middle Bastion
184 Ridge Formation (0 to 72 m, Fig. 4) is characterized by only small variation (-25.7 to 24.8 ‰) in
185 $\delta^{13}\text{C}_{\text{org}}$ with increasingly positive values towards the top at 70 m. The TOC values vary between
186 0.7 to 4.5 %. $\delta^{13}\text{C}_{\text{org}}$ values in the uppermost Bastion Ridge interval show a slight switch of 1‰
187 to more negative values at about 95 m, corresponding to low TOC values of close to 1 %. The
188 uppermost 7 m of the Bastion Ridge Formation (105 to 112 m) show an increase of ~0.5 ‰ to
189 more positive values (Fig. 4). Just above the basal boundary of the Kanguk Formation at 112 m a
190 significant, short-lived positive $\delta^{13}\text{C}_{\text{org}}$ excursion of 2 ‰ is coupled with the onset of organic-
191 rich platy shale and significant, but brief increase in TOC (10.9 %). Initially, this sustained
192 increase in TOC content corresponds to a strong negative excursion of 1.5 ‰ in the interval
193 between 122 to 130 m. The most significant positive $\delta^{13}\text{C}_{\text{org}}$ excursion of >2 ‰ representing
194 OAE2 occurs in the lower Kanguk Formation between 131 to 152 m and is accompanied with
195 elevated, but fluctuating TOC values of up to 10 %. Above 152 m $\delta^{13}\text{C}_{\text{org}}$ values stay initially
196 light and become gradually heavier throughout the middle to upper Turonian interval.

197 The Re abundance of the Bastion Ridge Formation shows little variation (0.2 to 1.2 ppb;
198 Fig. 4; Table 3). Noticeable enrichments in Re abundance are shown by a minor peak at 112 m of
199 5.2 ppb at the base of the Kanguk Formation, and in the ~127 m interval where Re increases to
200 13.3 ppb and then decreases to ~1-3 ppb. The ^{192}Os abundance profile (the best estimate of Os
201 chelated at the time of deposition) shows a similar trend to that of Re. In that, the ^{192}Os

202 abundance is relatively uniform within the Bastion Ridge Formation (5 to 40 ppt; Fig. 4; Table
203 3). As shown for Re in the ~127 m interval, a significant increase in ^{192}Os (up to 388 ppt) is
204 observed. However, no ^{192}Os enrichment is observed at the 112 m level where an enrichment in
205 Re of 5.2 ppb is shown.

206 In contrast to the Re and Os abundances, the initial $^{187}\text{Os}/^{188}\text{Os}$ (Os_i) compositions
207 through the Bastion Ridge and Kanguk formations are distinctly different. The Os_i values are
208 calculated at 94 Ma. As discussed above and below, part of the Bastion Ridge Formation is
209 appreciably older (~98 Ma) however, given the overall low Re abundance of the samples from
210 the Bastion Ridge Formation, the additional age correction equates to a difference smaller than
211 the uncertainty in the Os_i value (Table 3). As such, the Os_i profile shown in Figure 4 remains
212 essentially the same.

213 In the Bastion Ridge Formation between 5 and 25 m the Os_i compositions are relatively
214 uniform at ~0.55 (Fig. 4). From ~25 to 65 m the Os_i values become increasing more radiogenic
215 reaching a maximum of ~0.7. The Os_i values become less radiogenic over the following ~10 m,
216 to just beneath the freshwater siderite (Ross et al., 2018).

217 From the intervals at 87 to 105 m in the upper Bastion Ridge Formation the Os_i values
218 become increasingly more radiogenic (~0.4 to 0.6), and then become slightly more less
219 radiogenic to 111 m where the Os_i values show an abrupt shift to ~0.2 and return to ~0.4, where
220 the Os_i then exhibit a very nonradiogenic shift to ~0.1 at 114 m in the basal Kanguk Formation.
221 From 114 m the Os_i values abruptly return to radiogenic value of 0.70 for 10 m, and then at 125
222 m become nonradiogenic within the negative pronounced trend of the $\delta^{13}\text{C}$ profile and below the
223 abrupt positive $\delta^{13}\text{C}$ excursion interpreted that marks the onset of the OAE2 interval.

224 Nonradiogenic O_{s_i} compositions ($O_{s_i} = \sim 0.2$) continue for ~ 20 m before returning to more
225 radiogenic compositions of ~ 0.7 (Fig. 4; Table 3).

226 *3.2. Geochemical cycling*

227 Here we apply, Zn/Al and Mn/Al and Fe records to investigate magmatic/hydrothermal
228 contributions (Liao et al., 2018) to the Bastion Ridge and Kanguk formations (Fig. 4). The Zn/Al
229 distribution is variable throughout the section with consistently highest values in the uppermost
230 silty mudrock interval of the Bastion Ridge Formation (up to 100) and one peak (82) in the upper
231 interval of OAE2 (141 m) and a minor increase (17) at about 180 m within an interval marked by
232 numerous interbedded bentonite horizons. The Mn/Al values show two peaks at the base of and
233 in the uppermost Bastion Ridge Formation, correlating with the increased Zn/Al record. The
234 Zn/Al and Mn/Al records both show a significant increase at the base of the negative $\delta^{13}C$
235 excursion. The Fe abundance peaks at the base of the Bastion Ridge Formation (1 and 5 m) and
236 is elevated between 50 - 70 m (Fig. 4). Ratios of TOC (%) / Sulfur content (%) are plotted to
237 distinguish between marine and freshwater or slightly brackish regimes (Bernier and Raiswell,
238 1984). A higher ratio within the Bastion Ridge Formation confirms its brackish to freshwater
239 nature compared to the marine Kanguk Formation. The lowermost two samples in the Bastion
240 Ridge Formation form the exception indicating short-lived marine influence (Fig. 5).

241 *3.3. Foraminifera, palynomorph and paleoproductivity records*

242 The presence/absence of benthic foraminifera and their morphotype distribution permits
243 evaluation of benthic redox conditions (Nagy, 1992; Jorissen et al., 1995; Herrle et al., 2003;
244 Murray et al., 2011; Quesnel et al., 2017), which can then be compared with the carbon burial
245 history (Fig. 6). Only benthic foraminifera were recovered from the sample set and are absent in

246 intervals dominated by terrestrial and freshwater conditions such as most of the Bastion Ridge
247 Formation (4 to 112 m). Two additional barren intervals are notable; these are within the interval
248 of the lower positive carbon isotope excursion at ~112 m and right after OAE2 at 145 – 155 m,
249 but not within the OAE2 interval (Fig. 6).

250 Three morphotypes were distinguished (Fig. 6) including: a) infaunal deposit feeders with
251 elongated, multichambered tests, preferring mesotrophic to eutrophic environments that are often
252 oxygen-poor; b) shallow infaunal to epifaunal deposit feeders with coiled tests, adapted to
253 oxygenated, oligotrophic conditions; and c) epifaunal assemblages dominated by the genus
254 *Trochammina*, tolerant to reduced benthic oxygen conditions under high organic matter supply
255 (Gooday et al., 2000). The limited presence of benthic foraminifera at the base of the Bastion
256 Ridge Formation indicates a short marine phase which confirms the low marine TOC/S ratios in
257 those samples (Figs. 5, 6). The ‘paper shale’ unit of the basal Kanguk Formation including the
258 OAE2 interval is dominated by epifaunal taxa with minute tests, mainly of the genus
259 *Trochammina*. This genus has previously been related to depleted oxygen conditions of the
260 Toarcian Oceanic Anoxic Event (Reolid et al., 2014). Toward the top of OAE2 the highest
261 concentration of Mo (up to 8 ppm) occurs, a redox-sensitive trace metal that is enhanced under
262 sulfidic conditions (Helz et al., 1996). This interval (145 to 150 m) coincides with a reduction in
263 benthic fauna that does not recover for some time after OAE2 (Fig. 6). Finally, the upper
264 Turonian interval is characterized by increasingly diverse assemblages with all three
265 morphotypes represented (Fig. 6).

266 The uppermost Bastion Ridge Formation is dominated by the non-marine dinocysts
267 *Nyktericysta* sp. and *Vesperopsis* sp. of freshwater and brackish origin (Mao et al., 1999). The
268 non-marine acritarch *Limbicysta* sp. (MacRae et al. 1996) also has a common occurrence within

269 this interval; thereby, clearly confirming the placement of a terrestrially influenced unit in the
270 uppermost Bastion Ridge Formation. As the lithology changes to ‘paper shale’ in the basal
271 Kanguk Formation non-marine dinocysts and acritarchs disappear. Marine dinocysts appear in
272 small numbers with abundant amorphous organic matter. Pollen are abundant, and the interval
273 marked by the first pronounced negative $\delta^{13}\text{C}_{\text{org}}$ excursion is particularly dominated by wind-
274 blown bisaccates (Mudie, 1982). Within the actual OAE2 interval bisaccates lose their
275 dominance.

276 Hydrogen Indices (HI) vary around 50 mgCO_2/gOC in the Bastion Ridge Formation
277 supporting a terrestrial source. Within the Kanguk Formation HI values increase, ranging from
278 300 and 400 mgCO_2/gOC and coinciding with peaks in TOC at 114 m and within OAE2
279 suggesting an increasing marine organic matter source. At 170 m HI values return to terrestrial
280 signals (Fig. 6).

281 **4. Age Model of the Cenomanian/Turonian interval at Glacier Fiord**

282 The stratigraphic age model for the Glacier Fiord section is based on extrapolation using
283 proposed sedimentation rates where from 167 to 203 m five bentonite beds yield weighted
284 $^{206}\text{Pb}/^{238}\text{U}$ zircon CA-ID-TIMS dates of 93.03 ± 0.21 to 91.02 ± 0.3 Ma (Fig. 4; Davis et al.,
285 2016). A sedimentation rate of 19 m Ma^{-1} is calculated (Davis, et al., 2016) for the strata between
286 the oldest dated bentonite (93.03 ± 0.21 Ma) and the established age of the
287 Cenomanian/Turonian boundary (93.9 Ma) (Gradstein et al., 2012; Meyers et al., 2012; Du
288 Vivier et al., 2015) as placed close to the top of the OAE2 interval at 151 m. Lithologies in the
289 lower Kanguk interval are relatively even dominated by ‘paper shale’ with the occasional silty
290 interbeds suggesting a similar sedimentation rate of 19 m Ma^{-1} throughout. It is noted, however,

291 that some uncertainty could be caused by the position of the lowest dated bentonite within two
292 covered intervals where exact measurement of the section thickness might be slightly obscured.

293 Using the sedimentation rate of 19 m Ma^{-1} an approximate age of six intervals associated
294 with significant changes in the $\delta^{13}\text{C}_{\text{org}}$ and Os_i records are calculated (Fig. 4). These include in
295 ascending stratigraphic order: 1) the base of the Kanguk Formation at 112 m and onset of ‘paper
296 shale’ at $\sim 95.92 \text{ Ma}$ (level F); 2) the horizon at 114 m with the peak in TOC, $\delta^{13}\text{C}_{\text{org}}$ and non-
297 radiogenic Os_i pulse at $\sim 95.81 \text{ Ma}$ (level E); 3) the horizon at 125 m reflecting the first non-
298 radiogenic Os_i value from the prolonged non-radiogenic signal at $\sim 95.24 \text{ Ma}$ (level D); 4) the
299 base of the positive $\delta^{13}\text{C}$ excursion at 131 m interpreted as OAE2 at $\sim 94.92 \text{ Ma}$ (level A); 5) the
300 interval of the first slight negative shift in $\delta^{13}\text{C}$ at 137 m within OAE2 at $\sim 94.6 \text{ Ma}$ (level B); and
301 6) the top of OAE2 at 151 m where the $\delta^{13}\text{C}$ values return to more negative at $\sim 93.87 \text{ Ma}$ (level
302 C).

303 Globally the positive $\delta^{13}\text{C}$ values of OAE2 is described with three datum levels
304 (maintained here), where A marks the base of the positive excursion, B a trough after the first
305 positive excursion and C the level of the last positive $\delta^{13}\text{C}$ value (Pratt et al., 1985; Tsikos et al.,
306 2004; Forster et al., 2007). Using the latest $^{206}\text{Pb}/^{238}\text{U}$ zircon CA-ID-TIMS calibrated ages (Du
307 Vivier et al., 2015), the first least nonradiogenic Os_i value dated at $\sim 94.44 \pm 0.14 \text{ Ma}$ falls
308 stratigraphically below Datum A and being hence a few tens of thousands of years younger. This
309 agrees with the interpolated age from the Western Interior Seaway (WIS) OAE2 section (Meyers
310 et al., 2012; Du Vivier et al., 2015; Kuhnt et al., 2017). These dates coupled with the timing of
311 Datum C (93.92 Ma) yield an OAE2 duration of approximately 600 kyr years (Meyers et al.,
312 2012; Du Vivier et al., 2015). In contrast, notwithstanding argument of inheritance within the
313 CA-ID-TIMS zircon ages, constraints of the OAE2 interval of the Iona-1 core of western Texas,

314 USA extended the duration of OAE2 to approximately 900 kyr moving the base down to include
315 what Eldrett et al. (2014) called the precursor events of OAE2 (Jenkyns et al., 2017).

316 The importance of these calculated dates at the Glacier Fiord section results in the
317 exclusion of the positive excursion in $\delta^{13}\text{C}_{\text{org}}$ at 114 m from the OAE2 interval (Fig. 4). This
318 isotopically heavy carbon value at 114 m, although represented only by one measurement, is
319 significant given that a time equivalent environmental perturbation is also recognized by a
320 significant increase in TOC (~11 %), a clear shift to non-radiogenic Os_i and an increase in Re
321 abundance (Fig. 4). As the shale lithology persists down to 112 m in the section we use the same
322 sedimentation rate of 19 m Ma^{-1} , to place the $\delta^{13}\text{C}_{\text{org}}$ excursion at ~95.81 Ma (Level E).

323 Further, proposing an absolute age framework for the Bastion Ridge Formation becomes
324 more difficult due to the disconformities of unknown duration that would be associated with the
325 uppermost Bastion Ridge Formation (86 to 110 m) and markedly changing lithologies within the
326 formation. The proposed age of approximately 96 Ma for the base of the Bastion Ridge
327 Formation (Herrle et al., 2015) requires revision. A bentonite at 50 m within the middle of the
328 Bastion Ridge Formation yields a weighted average $^{206}\text{Pb}/^{238}\text{U}$ zircon CA-ID-TIMS minimum
329 age of $<98.3 \pm 1.8 \text{ Ma}$ (Davis et al., 2016) suggesting that the basal boundary could be closer to
330 the Albian/Cenomanian boundary (100.5 Ma; Gradstein et al., 2012) and the hiatus might be of
331 small duration.

332 Based on the youngest dated bentonite unit, the upper part of the Glacier Fiord section
333 studied here is younger than $91.02 \pm 0.3 \text{ Ma}$ (Davis et al., 2016). Biostratigraphic markers of
334 *Scaphites corvensis* and *S. nigricollensis* at 240 m in the upper Glacier Fiord section suggests a
335 latest Turonian age (~90.5 Ma; Schröder-Adams et al., 2014).

336 5. Discussion

337 The Cenomanian/Turonian boundary interval at Glacier Fiord offers a locality in close
338 vicinity to contemporaneous magmatic activities of the younger HALIP phases. In localities
339 north of Glacier Fiord, where the Strand Fiord volcanics are mapped (Fig. 1), the Bastion Ridge
340 Formation occurs either below the volcanics or interfingers with the volcanics (Fig. 3; Ricketts et
341 al., 1985; MacRae et al., 1996; Williamson, 2016). The Kanguk Formation conformably to
342 unconformably overlies the Strand Fiord Formation. Thus, the likelihood of direct magmatic
343 control on ocean geochemistry and local ecosystems is high. The interaction between basin
344 events, geochemical cycling and biotic response is discussed for five distinct stages that mark the
345 Cenomanian to Turonian interval in this polar locality.

346 5.1. Bastion Ridge Formation – tectonic setting and paleoenvironment

347 Stratigraphically, the regionally restricted Bastion Ridge Formation is time equivalent
348 with the upper Hassel Formation elsewhere (Fig. 2). Our reconstructions at Glacier Fiord place a
349 Cenomanian age on the Bastion Ridge Formation. On Ellef Ringnes Island (Fig. 1A), the Hassel
350 Formation ranges up into the Cenomanian (Galloway et al., 2012; Pugh et al., 2014), and it is the
351 Cenomanian part that is equivalent to the Bastion Ridge Formation (Fig. 2). Whereas the
352 surrounding Hassel Formation represents extensive shoreface, and deltaic deposits, the tectonic
353 and depositional paleoenvironment of the Bastion Ridge Formation is interpreted as a restricted
354 basin possibly related to a graben structure resulting in a protected embayment as the result of
355 tectonic basin extension (Embry and Osadetz, 1987; MacRae, 1992). This restricted basin was
356 marine in its initial phase supporting a foraminiferal assemblage (Fig. 6; Schröder-Adams et al.,
357 2014), but became more brackish and terrestrial up section (Fig. 5) with increasing amounts of
358 brackish acritarchs and terrestrial pollen, respectively (MacRae et al., 1996). This interpretation

359 is supported by the Os_i values, whereby the Os_i values become increasingly more radiogenic
360 from a background value of ~ 0.5 to 0.8 . The increasingly terrestrial nature of the Bastion Ridge
361 Formation is explained by uplift and possibly doming associated with the coeval eruption of the
362 Strand Fiord basalts (Dostal and MacRae, 2017) resulting in basin restriction. Phases of Mn, Zn
363 and Fe enrichment (Fig. 4) at the base of the Bastion Ridge Formation might be explained by
364 hydrothermal activity in the marine phase of the rift basin (German and Von Damm, 2006).
365 Later, geochemical signatures were also influenced by weathering of the surrounding Strand
366 Fiord volcanics as their eruptions might have further restricted the basin from marine influence.
367 Low TOC content and HI values (Fig. 6) point towards low to non-existing marine productivity
368 confirming faunal interpretations and low terrestrial organic matter input due to surrounding
369 volcanics without vegetation. The $\delta^{13}C_{org}$ record lacks any perturbations in a time where only
370 one preserved bentonite attests to a relatively quiet phase of volcanism throughout the early
371 Cenomanian. The overlying sandstone between 70 and 80 m is interpreted as a shoreface
372 sandstone, where bioturbation suggests a brief return to marine influence. This influence is
373 recorded in the Os_i values, where they become slightly less radiogenic. Within the middle
374 Cenomanian uppermost Bastion Ridge Formation freshwater siderite beds developed (Ross et al.,
375 in press). The presence of acritarchs gives evidence for intermittent brackish water influence and
376 coincide with more radiogenic Os_i values (~ 0.5 to 0.7).

377 Of interest in this interval is the $\delta^{13}C_{org}$ record which initially shows a couple of negative
378 excursions followed by a minor short-lived positive one between 108 and 110 m. Since the
379 overlying boundary between the Bastion Ridge/Kanguk formations is dated at ~ 95.92 Ma this
380 switch to positive $\delta^{13}C_{org}$ values falls closely to the age of the Mid-Cenomanian Event (MCE)
381 with an age of ~ 96 Ma (Paul et al. 1994; Jarvis et al., 2006; Joo and Sageman, 2014; Zhang et al.,

2016). The position of this interval in the uppermost terrestrial Bastion Ridge Formation (Fig. 6) might explain the weak positive $\delta^{13}\text{C}$ expression caused by terrestrial influence. Thus, correlation to marine MCE records elsewhere remains tentative. This event is immediately followed by a minor shift towards non-radiogenic Os_i values marked by level F and dated at 95.92 Ma (Fig. 4).

5.2. Kanguk Formation – the early transgressive phase

Embry and Osadetz (1988) assigned an approximate age of 95 Ma to the transition of the main rifting phase of the Canada Basin to a time of seafloor spreading, which consequently lasted for the next 25 myr (Fig. 2). At Glacier Fiord the upper Middle Cenomanian lithological change to marine ‘paper shale’ at 112 m in the section (Figs. 2, 3A, 4, 6) marks a phase of major basin subsidence and rapid transgression transforming this site into a shelf environment largely below storm wave base. Basin wide, the basal boundary of the Kanguk Formation is diachronous by using the position of the OAE2 positive carbon excursion as a chronostratigraphic marker (Davies et al., 2018). At Glacier Fiord the base of the Kanguk Formation falls at ~ 95.92 Ma. The depositional change is followed by a short lived positive $\delta^{13}\text{C}_{\text{org}}$ perturbation (level E at ~95.81 Ma, Fig. 4). Organic matter of dominantly terrestrial origin (Type III) swept into the basin through a transgressive shoreline (Fig. 6). A phase of increased paleoproductivity including marine dinoflagellates, stimulated by increased nutrient supply, and terrestrial organic matter input extended the oxygen minimum zone, which resulted into absence of benthic foraminifera. Relative abundance of wind-blown bisaccates decrease in abundance and terrestrially derived pollen increase. At the same time, a single sample shows a significant change to non-radiogenic Os_i values, a minor peak in Re abundance, but no change in ^{192}Os abundance. This is interpreted as the result of flooding the extensive Strand Fiord volcanics as a source of non-radiogenic Os. The organic-rich nature of this interval may explain the peak in Re as it acted as a sink for

405 dissolved Re in seawater (Jaffe et al., 2002). The return to radiogenic Os_i at 116 m correlates to
406 an interval dominated by siltstone beds pointing towards increased crustal weathering and greater
407 shoreline proximity.

408 *5.3. A negative carbon isotope excursion - a precursor to the Arctic OAE2 interval*

409 Level D (Fig. 4) dated at ~95.24 Ma is marked by the return to non-radiogenic Os_i , a peak
410 in ^{192}Os and Re abundance. This age closely correlates to the $^{40}Ar/^{39}Ar$ age of 95.3 ± 0.2 Ma
411 from the uppermost lava flow at Strand Fiord (Tarduno et al., 1998) and the age of 95.18 ± 0.35
412 Ma and 95.41 ± 0.12 Ma of two separate feeder dykes related to the late Strand Fiord HALIP
413 pulse (Kingsbury et al., 2018) suggesting a possible link and local influence (Fig. 4). The non-
414 radiogenic Os_i excursion at ~125 m places stratigraphically below the well-documented global
415 signature of non-radiogenic Os_i at the base of OAE2 with a younger age of ~94.4 Ma, which is
416 followed by a gradual return to radiogenic values (Du Vivier et al., 2014, 2015). The earlier
417 signal might be explained by local basin processes and/or age uncertainties of the Arctic site.

418 Level D is within a distinct negative $\delta^{13}C_{org}$ excursion that precedes the OAE2 positive
419 excursion. The upper shift to non-radiogenic Os_i values between 120 to 125 m corresponds
420 directly with the base of the negative $\delta^{13}C_{org}$ trend. The timing of this shift roughly corresponds
421 to established ages of the late Strand Fiord HALIP pulse (Kingsbury et al., 2018). Two scenarios
422 might explain the shift to non-radiogenic Os_i . If magmatism was submarine at this time
423 hydrothermal fluids were injected into the ocean. If the HALIP pulse was dominantly subaerial,
424 the Os record provides a weathering signal. The most negative $\delta^{13}C_{org}$ interval at Glacier Fiord
425 corresponds with the appearance of the first of several bentonites that become more common
426 during OAE2 alluding to nearby volcanism of possible HALIP origin. One explanation for this
427 shift to negative values might entail methane release due to mantle-derived intrusions into

428 organic-rich sediments of the Kanguk Formation (Fig. 4). Rapid heating of organic matter
429 through intrusive activity might have caused contact metamorphism and triggered sharp negative
430 carbon excursions caused by release of ^{13}C depleted carbon gases such as methane. A similar
431 mechanism is reported from the Toarcian Oceanic Anoxic Event and Early Eocene climate
432 maximum (Svensen et al., 2004, 2009; Aarnes et al., 2011). Detailed correlations between these
433 processes in the Sverdrup Basin require additional data and a more refined timeframe.

434 The distinct negative $\delta^{13}\text{C}$ excursion below OAE2 as seen at Glacier Fiord at ~95 Ma
435 appears to be only broadly contemporaneous with a distinct negative $\delta^{13}\text{C}$ excursion that
436 straddles the Middle to Late Cenomanian Boundary in the Natih Formation, Oman, which
437 consists of interbedded argillaceous and carbonate sediments (Wohlwend et al., 2016). Local
438 diagenetic processes within an intra-platform basin including sulphate reduction and anaerobic
439 oxidation of methane are invoked to cause the carbonates to be depleted in ^{13}C . As such
440 additional Arctic records are needed to pinpoint the cause and possible connection with the
441 HALIP phase.

442 *5.4. The polar OAE2 interval*

443 The positive $\delta^{13}\text{C}_{\text{org}}$ excursion denoting OAE2 is clearly expressed in the Glacier Fiord
444 section and is marked with the traditionally used levels of A, B and C (Fig. 4). As magmatic
445 activity and methane release ceased the carbon isotope signal resembles the global one. Its earlier
446 diachronous base compared to the Yezo Group of Japan, the Greenhorn Formation of the
447 Western Interior of the USA, and the OAE2 section in core SN°4 of the Tafaya Basin, Morocco
448 (Fig. 4, Du Vivier et al., 2015; Kuhnt et al., 2017) might be the result of some local influence on
449 the $\delta^{13}\text{C}_{\text{org}}$ record. Influences in restricted basins might include surface water productivity, input

450 of organic matter from land, remineralization in the water column, carbonate and organic
451 composition of the sediments and sea-level changes (Wagner et al., 2018 and references therein).
452 The change to more positive $\delta^{13}\text{C}_{\text{org}}$ values is rapid and the lithology does not show any evidence
453 for a disconformity. The age of Level B denotes a trough in the positive $\delta^{13}\text{C}_{\text{org}}$ excursion and
454 falls at ~94.6 Ma. At this interval the Os_i gradually return to radiogenic signatures. Further,
455 benthic foraminifera increase in diversity and abundance at this level which suggests an
456 increasingly oxygenated basin. This coincides with a drop in TOC and HI values (Fig. 6).
457 Although we have no Cenomanian/Turonian aged paleotemperature data from the Sverdrup
458 Basin, combined evidence shows that the Plenus Cold Event can be detected. Paleotemperature
459 proxies (TEX_{86}) have established a cooling trend at level B within the equatorial Atlantic
460 (Sinninghe Damsté et al., 2010; van Helmond et al., 2013).

461 Level C marks the top of OAE2 and an abrupt return to lighter carbon isotopes. Although
462 this abrupt change could suggest the presence of a hiatus, no lithological evidence for erosion
463 was discovered. Above this level TOC content and HI values remain relatively high for another
464 10 m within the lower Turonian. A comparable relatively abrupt change to increasingly more
465 negative $\delta^{13}\text{C}_{\text{org}}$ values was described from the Demarara Rise of the western equatorial Atlantic
466 (Forster et al., 2007) where interval C marks the recovery phase above the C/T boundary. Their
467 equatorial paleotemperature values denote a continued high sea surface temperature for the lower
468 Turonian. At Glacier Fiord moderate HI values reaching up to 350 mgCO_2/gOC , abundant
469 amorphous organic matter and a relatively poor, but diverse, marine dinoflagellate assemblage
470 suggests a sustained input of terrestrial material into the basin throughout OAE2 that was
471 supported by a climate regime of a warm and vegetated Arctic. At the Cenomanian/Turonian
472 boundary interval at May Point (Axel Heiberg Island, Fig. 1B), a persistently anoxic water

473 column was interpreted based on Fe_{Hf}/Fe_T data (Lenniger et al., 2014). At Glacier Fiord, benthic
474 foraminiferal assemblages are characterized by reduced species richness and in some samples a
475 dominance of epifaunal minute *Trochammina* specimens indicating stressed benthic
476 paleoenvironments in suboxic conditions. Varying TOC values throughout the OAE2 interval
477 might indicate a combination of varying supply of organic matter including marine productivity
478 and shifting redox conditions.

479 *5.5. Middle to Late Turonian – cooling and benthic recovery*

480 In the middle to upper Turonian interval lithologies have an increased abundance of silt
481 and are interbedded with frequent bentonite beds resulting partially from the Wootton Intrusive
482 Complex on Ellesmere Island (92.7 ± 0.3 Ma to 92 ± 0.1 Ma, Estrada and Henjes-Kunst, 2013)
483 or from another volcanic phase in the Amerasia Basin (Davis et al., 2016). The $\delta^{13}C_{org}$ gradually
484 increase towards more positive values and low TOC values suggest a more oxygenated ocean
485 under globally cooler conditions (Friedrich et al., 2012). Benthic foraminiferal assemblages
486 become more diverse with different morphotypes (Fig. 6). HI values give no indication for
487 marine primary productivity possibly inhibited by increasingly abundant detrital material in
488 surface waters. The peak in zinc enrichment between 180 and 200 m (Fig. 4) that coincides with
489 the interval of frequent bentonite occurrences might be the result of the capacity of bentonites to
490 absorb zinc (Sheta et al., 2003).

491 **6. Conclusions**

492 The Arctic Sverdrup Basin is the partial locale of the HALIP, a magmatic event that was
493 suggested besides the Caribbean LIP as a controlling force for the oceanic osmium isotope
494 stratigraphic profile within the Cenomanian/Turonian boundary interval. Correlations between

495 Os_i and $\delta^{13}C_{org}$ records mark a rapid shift to non-radiogenic Os_i values at the base of the OAE2
496 interval in open ocean settings suggesting LIP emplacement as one of the trigger mechanisms for
497 OAEs. Smaller basins show the accentuation of precursor signals that might refer to local
498 processes. This study makes the first direct comparison between ocean geochemical profiles and
499 HALIP phases for an Arctic Cenomanian/Turonian boundary interval and reveals the sensitivity
500 of ocean chemistry within a complex basin setting.

501 1. The dominantly brackish to terrestrial Bastion Ridge and marine Kanguk formations at Glacier
502 Fiord provide a polar paleoenvironmental response to the globally recognized Cenomanian to
503 Turonian carbon perturbations in close vicinity to one of the major LIP events, namely the Strand
504 Fiord phase of the HALIP. The sequence of two events, as clearly displayed in carbon and
505 osmium isotopic records, makes an argument for the control of local magmatic events on
506 chemical cycling and ecosystem response within this High Arctic Cenomanian/Turonian
507 boundary interval.

508 2. The basal interval of the Kanguk Formation records two phases of non-radiogenic osmium
509 input; the first at ~95.8 Ma was short lived interpreted as a product of weathering of the Strand
510 Fiord volcanics, that formed a topographic high at the time of Kanguk transgression. The second
511 phase at ~95.2 Ma with a gradual return to radiogenic Os_i values represents the open ocean
512 signal of a LIP and coincided with a major pulse of the Strand Fiord volcanics that were extruded
513 near to the Glacier Fiord locality. Additional data are required to calibrate the Arctic record
514 partially driven by local processes, with the global, open ocean record.

515 3. As in other restricted basins the polar Sverdrup Basin accentuated a local signal of a distinct
516 negative carbon isotope excursion that predated the global signal of the OAE2 which might have

517 been the result of coeval intrusion of mantle-derived material into organic-rich shale causing
518 carbon dioxide and methane release.

519 4. Ultimately global climate warmed and increasing amounts of marine and terrestrially derived
520 organic matter was buried in the Sverdrup Basin resulting in a distinct positive carbon isotope
521 excursion identified as OAE2 in the Arctic with a minimum duration of ~0.5 myr.

522 5. Benthic foraminifera and their morphogroup distributions allude to a basin of variable benthic
523 redox conditions throughout its fully marine phases. Whereas anoxic phases barren of
524 foraminifera existed, these did not occur during the OAE2 interval. There, assemblages of
525 epifaunal species, tolerant to relatively low bottom water oxygen conditions, persisted giving
526 testimony to suboxic conditions that still supported life.

527 The Glacier Fiord record is the first attempt to link carbon and osmium isotope records to
528 the HALIP phase and consequently has constrained the Late Cretaceous Arctic stratigraphic
529 framework. Our data has shed light on the complex interplay between subaerial versus submarine
530 magmatic events, their linkage to regressive/transgressive phases; paleoceanographic responses
531 to methane release and hydrothermal activity and ecosystem response. Our interpretations
532 require future testing in the Sverdrup, Amerasia and Eurasia basins to evaluate further the
533 influence of HALIP phases on paleoceanographic events. Future correlations require reliable age
534 frameworks which then will allow increasingly global correlations and the identification of
535 dominant large-scale earth processes.

536

537 **Acknowledgement**

538 We are grateful to the Nunavut Research Institute, Nunavut Water Board and Nunavut
539 Department of Culture and Heritage for granting us the scientific research licenses. We like to
540 thank the community of Grise Fiord for their agreement to conduct research on northern lands.
541 Keenan Lindell is thanked for valuable field support and Craig Day for discussions on
542 geochemical data. Denise Then, Mark Bujaki and Global Geolab LTD are thanked for sample
543 preparation. Ross Stewart and Krista Boyce are thanked for Rock-Eval analysis. We thank Jens
544 Fiebig and Bärbel Schminke for stable isotope and TOC measurements. Alice Du-Vivier, Chris
545 Ottley, Geoff Nowell and Antonia Hofmann are thanked for laboratory support. We express our
546 sincerest gratitude to the reliable staff and pilots of the Polar Continental Shelf Program who
547 provided unfailing logistical support in the North. Two anonymous reviewers provided
548 constructive comments that improved the manuscript. Financial support to Schröder-Adams was
549 provided by a CRD Grant of the Natural Sciences and Engineering Research Council (NSERC)
550 with the Geo-mapping for Energy and Minerals (GEM) Program of the Geological Survey of
551 Canada and ConocoPhillips Houston and Calgary as partners. Financial support to Herrle was
552 provided by the German Research Foundation (DFG) (HE 3521/6). DS acknowledges the Total
553 Endowment Fund and the CUG Wuhan Dida Scholarship.

554

555 **References**

- 556 Aarnes, I., Svensen, H., Polteau, S., Planke, S., 2011. Contact metamorphic devolatilization of
557 shales in the Karoo Basin, South Africa, and the effects of multiple sill intrusions. *Chemical*
558 *Geology*, 281, 181-194.
- 559 Berner, R.A., Raiswell, R., 1984. C/S method for distinguishing freshwater from marine
560 sedimentary rocks. *Geology*, 12, 365-368.

- 561 Buchan, K.L., Ernst, R., 2006. Giant dyke swarms and the reconstruction of the Canadian Arctic
562 islands, Greenland, Svalbard and Franz Josef Land. In Hanski, E., Mertanen, S., Rämö, T.,
563 Vuollo, J. (eds.). Dyke swarms – Time markers of crustal evolution, Taylor & Francis,
564 London, p. 27-48.
- 565 Davies, M.A., Schröder-Adams, C.J., Herrle, J.O., Hülse, P., Schneider, S., Quesnel, A.,
566 Harwood, D., 2018. Integrated bio- and carbon isotope-stratigraphy for the Upper Cretaceous
567 Kanguk Formation of the High Arctic Sverdrup Basin, Canada. Geological Society of
568 America, Bulletin, DOI: 10.1130/B31858.1.
- 569 Davis, W.J., Schröder-Adams, C.J., Galloway, J.M., Herrle, J.O., Pugh, A.T., 2016. U-Pb
570 geochronology of bentonites from the upper Cretaceous Kanguk Formation, Sverdrup Basin,
571 Arctic Canada: constraints on sedimentation rates, biostratigraphic correlations and the late
572 magmatic history of the High Arctic Large Igneous Province. Geological Magazine, DOI:
573 [10.1017/S0016756816000376](https://doi.org/10.1017/S0016756816000376).
- 574 Dostal, J., MacRae, A., 2017. Cretaceous basalts of the High Arctic Large Igneous Province at
575 Axel Heiberg Island (Canada): Volcanic stratigraphy, geodynamic setting and origin.
576 Geological Journal, DOI:10.1002/gj.3132.
- 577 Du Vivier, A.D.C., Selby, D., Condon, D.J., Takashima, R., Nishi, H., 2015. Pacific $^{187}\text{Os}/^{188}\text{Os}$
578 isotope chemistry and U-Pb geochronology: Synchronicity of global Os isotope change across
579 OAE 2. Earth and Planetary Science Letters, 428, 204-216.
- 580 Du Vivier, A.D.C., Selby, D., Sageman, B.B., Jarvis, I., Gröcke, D.R., Voigt, S., 2014. Marine
581 $^{187}\text{Os}/^{188}\text{Os}$ isotope stratigraphy reveals the interaction of volcanism and ocean circulation
582 during Oceanic Anoxic Event 2. Earth and Planetary Science Letters, 389, 23-33.

- 583 Eldrett, J.S., Minisini, D., Bergman, S.C., 2014. Decoupling of the carbon cycle during Ocean
584 Anoxic Event 2. *Geology*, 42 (7), 567-570.
- 585 Embry, A., Beauchamp, B., 2008. Sverdrup Basin, In Miall, A. (ed.). *Sedimentary Basins of the*
586 *World, Volume 5, The Sedimentary Basins of the United States and Canada: Amsterdam,*
587 *Elsevier*, p. 451–472.
- 588 Embry, A.F., Dixon, J., 1990. The breakup unconformity of the Amerasia Basin, Arctic
589 Ocean: Evidence from Arctic Canada. *Geological Society of America Bulletin* 102,
590 1526–1534.
- 591 Embry, A.F., Osadetz, K.G., 1988. Stratigraphic and tectonic significance of Cretaceous
592 volcanism in the Queen Elizabeth Islands, Canadian Arctic Archipelago. *Canadian Journal*
593 *Earth Sciences*, 25, 1209-1219.
- 594 Erba, E., Duncan, R.A., Bottini, C., Tiraboschi, D., Weissert, H., Jenkyns, H.C., and Malinverno,
595 A., 2015. Environmental consequences of Ontong Java Plateau and Kerguelen Plateau
596 volcanism. In Neal, C.R., Sager, W.W, Sano, T., and Erba, E. (eds.), *The Origin, Evolution,*
597 *and Environmental Impact of Oceanic Large Igneous Provinces. Geological Society of*
598 *America Special Paper* 511, 271–303, doi:10.1130/2015.2511(15).
- 599 Ernst, R.E., Youbi, N., 2017. How Large Igneous Provinces affect global climate, sometimes
600 cause mass extinctions, and represent natural markers in the geologic record.
601 *Palaeogeography Palaeoclimatology Palaeoecology*, [DOI:10.1016/j.palaeo.2017.03.014](https://doi.org/10.1016/j.palaeo.2017.03.014).
- 602 Estrada, S., Damaske, D., Henjes-Kunst, F., Schreckenberger, B., Oakey, G.N., Piepjohn, K.,
603 Eckelmann, K., Linnemann, U., 2016. Multistage Cretaceous magmatism in the northern
604 coastal region of Ellesmere Island and its relation to the formation of Alpha Ridge-evidence

- 605 from aeromagmatic, geochemical and geochronological data. *Norwegian Journal of Geology*,
606 96 (2), 65-95.
- 607 Estrada, S., Henjes-Kunst, F., 2004. Volcanism in the Canadian High Arctic related to the
608 opening of the Arctic Ocean, *Zeitschrift Deutsche Geologische Gesellschaft*, 154, 579-603.
- 609 Estrada, S., Henjes-Kunst, F., 2013. ^{40}Ar - ^{39}Ar and U-Pb dating of the Cretaceous continental rift-
610 related magmatism on the northeast Canadian Arctic margin. *German Journal Geosciences*,
611 164 (1), 107-130.
- 612 Evenchick, C.A., Davis, W.J., Bédard, J.H., Hayward, N., Friedman, R.M., 2015. Evidence for
613 protracted high Arctic large igneous province magmatism in the central Sverdrup Basin from
614 stratigraphy, geochronology, and paleodepths of saucer-shaped sills. *GSA Bulletin*, DOI:
615 10.1130/B31190.1.
- 616 Forster, A., Schouten, S., Moriya, K., Wilson, P.A., Sinninghe Damsté, J.S., 2007. Tropical
617 warming and intermittent cooling during the Cenomanian/Turonian oceanic anoxic event 2:
618 Sea surface temperature records from the equatorial Atlantic. *Paleoceanography*, 22,
619 PA1219, DOI:10.1029/2006PA001349.
- 620 Friedrich, O., Norris, R.D., Erbacher, J., 2012. Evolution of middle to Late Cretaceous oceans –
621 A 55 m.y. record of Earth's temperature and carbon cycle. *Geology*, DOI:10.1130/G32701.1.
- 622 Galloway, J.M., Sweet, A.R., Pugh, A., Schröder-Adams, C.J., Swindles, G.T., Haggart, J.W.,
623 Embry, A.F., 2012. Correlating middle Cretaceous palynological records from the Canadian
624 High Arctic based on a section from the Sverdrup Basin and samples from the Eclipse
625 Trough. *Palynology*, 36:2, 277-302.
- 626 German, C.R., von Damm, K.L., 2006. Hydrothermal processes. In Elderfield, H. (ed.), *The*
627 *Ocean and marine Geochemistry. Treatise on Geochemistry, Volume 6*, 181-222. Elsevier.

- 628 Gooday, A.J., Bernhard, J.M., Levin, L.A., Suhr, S., 2000. Foraminifera in the Arabian Sea
629 OMZ and other oxygen deficient settings: taxonomic composition, diversity and relation
630 to metazoan faunas. *Deep-Sea Research II*, 47, 25–54. DOI:10.1016/S0967-0645(99)00099-
631 5.
- 632 Gradstein, F.M., Ogg, J.G., Schmitz, M.D., Ogg, G.M., 2012. *The Geologic Time Scale 2012*,
633 Volume 2: Oxford, United Kingdom, Elsevier, 1144 p.
- 634 Helz, G.R., Miller, C.V., Charnock, J.M., Mosselmans, J.F.W.,
635 Pattrick, R.A.D., Garner, C.D., and Vaughan, D.J., 1996.
636 Mechanism of molybdenum removal from the sea and its
637 concentration in black shales: EXAFS evidence: *Geochimica et*
638 *Cosmochimica Acta*, 60, 3631–3642, DOI:10.1016/0016-
639 7037(96)00195-0.
- 640 Herrle, J.O., Pross, J., Friedrich, O., Hemleben, C., 2003. Short-term environmental changes in
641 the Cretaceous Tethyan Ocean: Micropaleontological evidence from the Early Albian
642 Oceanic Anoxic Event 1b. *Terra Nova*, 15, 14-19.
- 643 Herrle, J.O., Schröder-Adams, C.J., Davis, W., Pugh, A.T., Galloway, J.M., Fath, J., 2015. Mid-
644 Cretaceous High Arctic stratigraphy, climate, and Oceanic Anoxic Events. *Geology*, 43, 403-
645 406.
- 646 Holmden, C., Jacobson, A.D., Sageman, B.B., Hurtgen, M.T., 2016, Response of the Cr isotope
647 proxy to Cretaceous Anoxic Event 2 in a pelagic carbonate succession from the Western
648 Interior Seaway. *Geochimica et Cosmochimica Acta*, 186, 277-295.
- 649 Jaffe, A.L., Peucker-Ehrenbrink, B., Petsch, S.T., 2002. Mobility of rhenium, platinum group
650 elements and organic carbon during black shale weathering. *Earth and Planetary Science*
651 *Letters*, 198. 339-353.

- 652 Jarvis, I., Gale, A.S., Jenkyns, H.C., Pearce, M.A., 2006. Secular variation in the late Cretaceous
653 carbon isotopes: a new $\delta^{13}\text{C}$ carbonate reference curve for the Cenomanian–
654 Campanian (99.6–70.6 Ma). *Geological Magazine* 143, 561–608.
- 655 Jenkyns, H.C., Dickson, A.J., Ruhl, M., Van Den Boorn, S.H.J.M., 2017. Basalt-seawater
656 interaction, the Plenus Cold Event, enhanced weathering and geochemical change:
657 deconstructing Oceanic Anoxic Event 2 (Cenomanian-Turonian, Late Cretaceous).
658 *Sedimentology*, 64, 16-43.
- 659 Joo, Y.J., Sageman, B.B., 2014. Cenomanian to Campanian carbon isotope chemostratigraphy
660 from the Western Interior Basin, U.S.A. *Journal of Sedimentary Research*, 84, 529-542.
- 661 Jorissen, F.J., de Stigter, H.C., Widmark, J.G.V., 1995. A conceptual model explaining benthic
662 foraminiferal microhabitats. *Marine Micropaleontology*, 22, 3–15. DOI:10.
663 1016/0377-8398(95)00047-X.
- 664 Jowitt, S.M., Williamson, M., Ernst, R.E., 2014. Geochemistry of the 130 to 80 Ma Canadian
665 Arctic Large Igneous province (HALIP) event and implications for Ni-Cu-PGE
666 prospectivity. *Economic Geology*, 109, 281-307.
- 667 Kingsbury, C. G., Kamo, S. L., Ernst, R. E., Söderlund, U., Cousens, B. L., 2018. U-Pb
668 geochronology of the plumbing system associated with the Late Cretaceous Strand Fiord
669 Formation, Axel Heiberg Island, Canada: part of the 130-90 Ma High Arctic large igneous
670 province. *Journal of Geodynamics* [DOI: 10.1016/j.jog.2017.11.001](https://doi.org/10.1016/j.jog.2017.11.001).
- 671 Kuhnt, W., A.E. Holbourn, S. Beil, M. Aquit, T. Krawczyk, S. Flogel, E.H. Chellai, H. Jabour,
672 2017, Unravelling the onset of Cretaceous Oceanic Anoxic Event 2 in an extended sediment
673 archive from the Tarfaya-Laayoune Basin, Morocco, *Paleoceanography*, DOI:
674 10.1002/2017PA003146.

- 675 Lenniger, M., Nøhr-Hansen, H., Hills, L.V., Bjerrum, C.J., 2014, Arctic black shale
676 formation during Cretaceous Oceanic Anoxic Event 2. *Geology* 42, 799-802.
- 677 Liao, S., Tao, C., Li, H., Zhang, G., Liang, J., Yang, W., Wang, Y., 2018. Surface sediment
678 geochemistry and hydrothermal activity indicators in the Dragon Horn area on the Southwest
679 Indian Ridge. *Marine Geology*, 398, 22-34.
- 680 MacRae, R.A., 1992. Palynology of the Bastion Ridge and Strand Fiord formations, western
681 Axel Heiberg Island. Canadian Arctic Islands, N.W.T.: implications for stratigraphy, age,
682 paleoenvironment, and *Nyktericysta* taxonomy. M.Sc. thesis, University of Calgary, Alberta.
683 347 p.
- 684 MacRae, R.A., Hills, L.V., McIntyre, D.J., 1996. The paleoecological significance of new
685 species of *Limbicysta* (Acritarcha) from the upper Albian of the Canadian Arctic islands.
686 *Canadian Journal of Earth Sciences*, 33, 1475-1486.
- 687 Mao, S., Wan, C., Qiao, X., 1999. Cretaceous nonmarine dinoflagellates from northeast China.
688 *Grana*, 38, 144-161.
- 689 Meyers, S.R., Siewert, S.E., Singer, B.S., Sageman, B.B., Condon, D.J., Obradovich, J.D., Jicha,
690 B.R., Sawyer, D.A., 2012. Intercalibration of radioisotopic and astrochronologic time scales
691 for the Cenomanian-Turonian boundary interval, Western Interior Basin, USA. *Geology*, 40
692 (1), 7-10.
- 693 Murray, J.W., Alve, E., Jones, B.W., 2011. A new look at modern agglutinated benthic
694 foraminiferal morphogroups: their value in palaeoecological interpretation. *Palaeogeography,*
695 *Palaeoclimatology, Palaeoecology*, 309, 229-241.
- 696 Mudie, P.J., 1982. Pollen distribution in recent marine sediments, eastern Canada. *Canadian*
697 *Journal of Earth Sciences*, 19, 729-747.

- 698 Nagy, J., 1992. Environmental significance of foraminiferal morphogroups in Jurassic North Sea
699 deltas: *Palaeogeography, Palaeoclimatology, Palaeoecology*, 95, 111-134.
- 700 Núñez-Betelu, L.K., MacRae, R.A., Hills, L.V., Muecke, G.K., 1994. Uppermost Albian
701 Campanian palynological biostratigraphy of Axel Heiberg and Ellesmere islands
702 (Canadian Arctic). In: Thurston, D.K., Fujita, K. (eds.), *Proceedings of the 1992 International
703 Conference on Arctic Margins, Anchorage, Alaska*. U.S. Department of the
704 Interior, Anchorage, Alaska, p. 135–140.
- 705 Paul, C.R.C., Mitchell, S.F., Marshall, J.D., Leary, P.N., Gale, A.S., Duane, A.M., Ditchfield,
706 P.W., 1994. Palaeoceanographic events in the Middle Cenomanian of Northwest Europe.
707 *Cretaceous Research* 15, 707–738.
- 708 Pratt, L.M., Kauffman, E.G., Zelt, F.B., 1985. Fine-grained deposits and biofacies of the
709 Cretaceous Western Interior Seaway: Evidence for cyclic sedimentary processes. *Society
710 Economic Paleontology, Mineralogy Fieldtrip Guidebook 4, 1985 Midyear Meeting, Golden,
711 Colorado*.
- 712 Pugh, A.T., Schröder-Adams, C.J., Carter, E.S., Herrle, J.O., Galloway, J., Haggart, J.W.,
713 Andrews, J.L., Hatsukano, K., 2014. Cenomanian to Santonian radiolarian biostratigraphy,
714 carbon isotope stratigraphy and paleoenvironments of the Sverdrup Basin, Ellef Ringnes
715 Island, Nunavut, Canada. *Palaeogeography, Palaeoclimatology, Palaeoecology*, 413, 101-
716 122.
- 717 Quesnel, A., Schröder-Adams, C.J., Davies, W., 2017. Cretaceous (Albian to Cenomanian)
718 biostratigraphic, paleogeographic and paleoenvironmental reconstruction of the northern
719 Western Interior Sea: Yukon, Canada. *Palaeogeography, Palaeoclimatology, Palaeoecology*,
720 468, 453-472.

- 721 Reolid, M., Nikitenko, B.L., Glinskikh, L., 2014. *Trochammina* as opportunist foraminifera in
722 the Lower Jurassic from north Siberia. *Polar Research*, 33:1, DOI:10.3402/polar.v33.21653.
- 723 Ricketts, B., Osadetz, K.G., Embry, A.F., 1985. Volcanic style in the Strand Fiord Formation
724 (Upper Cretaceous), Axel Heiberg Island, Canadian Arctic Archipelago. *Polar Research*, 3,
725 107-122.
- 726 Ross, J.B., Ludvigson, G.A., Schröder-Adams, C.J., and Suarez, M.B., in press. High latitude
727 meteoric $\delta^{18}\text{O}$ compositions from the Cenomanian Bastion Ridge Formation, Axel Heiberg
728 Island, Canadian Arctic Archipelago: A paleoclimate proxy from the Sverdrup
729 Basin. In Wagreich, M., (ed.), *Cretaceous Climate Events and Short-Term Sea-Level*
730 *Changes*, Geological Society London, Special Publication.
- 731 Saumur, B.M., Dewing, K., Williamson, M.-C., 2016. Architecture of the Canadian portion of
732 the High Arctic Large Igneous Province and implications for magmatic Ni-Cu potential.
733 *Canadian Journal of Earth Sciences*, 53, 528-542.
- 734 Scaife, J.D., Ruhl, M., Dickson, A.J., Mather, T.A., Jenkyns, H.C., Percival, L.M.E., Hesselbo,
735 S.P., Cartwright, J., Eldrett, J.S., Bergman, S.C., Minisini, D. Sedimentary mercury
736 enrichments as a marker for submarine Large Igneous Province volcanism? Evidence from
737 the Mid-Cenomanian Event and Oceanic Anoxic Event 2. *Geochemistry, Geophysics,*
738 *Geosystems*, 18, 4253-4275.
- 739 Schröder-Adams, C.J., Herrle, J.O., Embry, A.F., Haggart, J.W., Galloway, J.M., Pugh, A.T.,
740 Harwood, D.M., 2014. Aptian to Santonian foraminiferal biostratigraphy and
741 paleoenvironmental change in the Sverdrup Basin as revealed at Glacier Fiord, Axel Heiberg
742 Island, Canadian Arctic Archipelago. *Palaeogeography, Palaeoclimatology, Palaeoecology*,
743 413, 81-100.

- 744 Sheta, A.S., Falatah, A.M., Al-Sewailem, M.S., Khaled, E.M., Sallam, A.S.H., 2003. Sorption
745 characteristics of zinc and iron by natural zeolite and bentonite. *Microporous and*
746 *mesoporous Materials*, 61, 127-136.
- 747 Sinninghe Damsté, J.S., van Bentum, E.C., Reichert, G.-J., Pross, J., Schouten, S., 2010. A CO₂
748 decrease-driven cooling and increased latitudinal temperature gradient during the mid
749 Cretaceous Oceanic Anoxic Event 2. *Earth and Planetary Science Letters*, DOI:
750 10.1016/j.epsl.2010.02.027.
- 751 Snow, L.J., Duncan, R.A., Bralower, T.J., 2005. Trace element abundances in the Rock
752 Canyon Anticline, Pueblo, Colorado, marine sedimentary section and their relationship
753 to Caribbean plateau construction and oxygen anoxic event 2. *Paleoceanography*
754 20, PA3005. DOI: 10.1029/2004PA001093.
- 755 Souther, J.G., 1963. Geological traverse across Axel Heiberg Island from Buchanan Lake to
756 Strand Fiord. *Geological Survey of Canada, Memoir* 320, 426-448.
- 757 Svensen, H., Planke, S., Polozov, A.G., Schmidbauer, N., Corfu, F., Podladchikov, Y.Y.,
758 Jamtveit, B., 2009. Siberian gas venting and the end-Permian environmental crisis. *Earth and*
759 *Planetary Science Letters*, 277, 490-500.
- 760 Svensen, H., Planke, S., Malthe-Sørensen, A., Jamtveit, B., Myklebust, R., Rasmussen Eidem,
761 T., Rey, S.S., 2004. Release of methane from a volcanic basin as a mechanism for initial
762 Eocene global warming. *Nature*, 429, 542-545.
- 763 Tarduno, J.A., Brinkman, D.B., Renne, P.R., Cottrell, R.D., Scher, H., Castillo, P., 1998.
764 Evidence for extreme climatic warmth from Late Cretaceous Arctic vertebrates. *Science*,
765 282, 2241-2244.

- 766 Tegner, C., Storey, M., Holm, P.M., Thorarinsson, S.B., Zhao, X., Lo, C.-H., Knudsen, M.F.,
767 2011. Magmatism and Eureka deformation in the High Arctic Large Igneous Province:
768 ^{40}Ar - ^{39}Ar age of Kap Washington Group volcanics, North Greenland. *Earth and Planetary*
769 *Science Letters*, 303, 203-214.
- 770 Thorarinsson, S.B., Holm, P.M., Tapper, S., Heaman, I.M., Tegner, C., 2011. Late Cretaceous-
771 Palaeocene continental rifting in the High Arctic: U-Pb geochronology of the Kap
772 Washington Group volcanic sequence, North Greenland. *Journal of the Geological Society*,
773 London, 168, 1093-1106.
- 774 Thorsteinsson, R., 1971. *Geology, Strand Fiord*. Geological Survey of Canada Map 1301A.
- 775 Tsikos, H., Jenkyns, H.C., Walsworth-Bell, B., Petrizzo, M.R., Forster, A., Kolonic, S., Erba, E.,
776 Premoli-Siva, I.P., Baas, M., Wagner, T., Sinninghe Damsté, J.S., 2004. Carbon-isotope
777 stratigraphy recorded by the Cenomanian-Turonian Oceanic Anoxic Event: correlation and
778 implications based on three key localities. *Memoir Geological Society of London*, 161, 711-
779 719.
- 780 Turgeon, S.C., Creaser, R.A., 2008. Cretaceous Anoxic Event 2 triggered by a massive magmatic
781 episode. *Nature*, 454, 323-326.
- 782 Van Helmond, N.A.G.M., Sluijs, A., Reichert, G.-J., Sinninghe Damsté, J.S., Slomp, C.P.,
783 Brinkhuis, H., 2013. A perturbed hydrological cycle during Oceanic Anoxic Event 2.
784 *Geology*, DOI: 10.1130/G34929.1.
- 785 Villeneuve, M., Williamson, M.-C. 2006. ^{40}Ar - ^{39}Ar dating of mafic magmatism from the
786 Sverdrup Basin Magmatic Province. In Scott, R.A., Thurston D.K. (eds.). *Proceedings of the*
787 *4th Int. Conf. on Arctic Margins (ICAM IV)*, 206-215, Anchorage Alaska. (OCS Study,
788 MMS 2006-003, U.S. Department of the Interior).

- 789 Wagner T., Magill C.R., Herrle J.O., 2018. Carbon Isotopes. In: White W. (eds.)
790 Encyclopedia of Geochemistry. Encyclopedia of Earth Sciences Series. Springer, Cham.
- 791 Williamson, M.-C., 1988. The Cretaceous igneous province of the Sverdrup Basin, Canadian
792 Arctic: Field relations and petrochemical studies. Ph.D. thesis, Dalhousie University,
793 Halifax, Nova Scotia. 417 p.
- 794 Williamson, M.-C., 2016. Report of Activities for High Arctic large Igneous Province (HALIP) –
795 GEM 2 Western Arctic Region project: Bedrock Mapping and Mineral Exploration.
796 Geological Survey of Canada Open File 7950, 48 p.
- 797 Wohlwend, S., Hart, M., Weissert, H., 2016. Chemostratigraphy of the Upper Albian to mid-
798 Turonian Natih Formation (Oman) – how authigenic carbonate changes a global pattern. The
799 Depositional Record, DOI: 10.1002/dep2.15.
- 800 Zhang, X., Chen, K., Hu, D., Sha, J., 2016. Mid-Cretaceous carbon cycle perturbations and
801 Oceanic Anoxic Events recorded in southern Tibet. Scientific Reports, 6, 39643, DOI:
802 10.1038/srep39643.
- 803 Zheng, X.-Y., Jenkyns, H.C., Gale, A.S., Ward, D.J., Henderson, G.M., 2013. Changing
804 ocean circulation and hydrothermal inputs during Oceanic Anoxic Event 2
805 (Cenomanian–Turonian): Evidence from Nd-isotopes in the European shelf sea.
806 Earth Planetary Science Letters. DOI: 10.1016/j.epsl.2013.05.053i.

807

808 **Figure Captions**

- 809 Figure 1: A) Locality map of Queen Elizabeth Islands, Canadian High Arctic. B) Map of Axel
810 Heiberg Island. Star indicates section locality at head of Glacier Fiord. The circled area shows

811 the approximate extent of the Strand Fiord Formation on Axel Heiberg Island (after Estrada and
812 Henjes-Kunst, 2013).

813 Figure 2: Stratigraphic framework of the upper Albian to Campanian interval based on sections
814 on Ellef Ringnes Island representing the basin centre (Pugh et al., 2014), Bunde Fiord and Strand
815 Fiord as the main localities of the Strand Fiord volcanics (Rickett et al., 1985, MacRae et al.,
816 1996), Glacier Fiord (Schröder-Adams et al., 2014 and this study) and Slidre Fiord, a marginal
817 basin position (Davies et al., 2018). The stratigraphic position of OAE2 as a timeline is known
818 from Slidre Fiord (Davies et al., 2018), Glacier Fiord (Herrle et al., 2015 and this study) and
819 Hoodoo Dome (Pugh et al., 2014). The presence of the OAE2 interval at Strand Fiord is
820 unknown. Bunde Fiord shows the thickest extent of Strand Fiord Formation, but no Kanguk
821 Formation is exposed (for localities see Fig. 1B). The age of the Kanguk transgression in these
822 localities is questionable. Note the diachronous basal boundary of the Kangak Formation.
823 Canada Basin Events after Embry and Osadetz (1988). Age of Wootton Intrusive Complex on
824 Ellesmere Island after Estrada and Henjes-Kunst (2013).

825 Figure 3: A) Measured and analyzed section at Glacier Fiord (red line). Arrow points toward the
826 sequence boundary at the Albian/Cenomanian Boundary at the base of the Bastion Ridge
827 Formation expressed as a thin paleosol. A second sequence boundary is expressed by freshwater
828 siderite beds within the upper Bastion Ridge Formation of middle Cenomanian age. The OAE2
829 interval in the lower Kanguk Formation is marked. The interval immediately above the upper
830 sandstone unit of the Bastion Ridge Formation is not well exposed on that side of the glacial
831 stream that flows in front of the section. In 2014 it was measured on the opposite stream cut, not
832 shown here. B) View from Lost Hammer Diapir of the Hassel Formation overlain by the flood
833 basalts of the Strand Fiord Formation north of Glacier Fiord. The regionally restricted Bastion

834 Ridge Formation is not exposed here. C) Close-up of middle Bastion Ridge Formation showing
835 the iron-rich sediments of the restricted basin, particularly in the upper half. A bioturbated
836 shoreface sandstone forms the ridge. D) Contact between the Strand Fiord volcanics and the
837 Kanguk Formation at Expedition Fiord (photo courtesy of Simon Schneider).

838 Figure 4: Measured section at Glacier Fiord after Schröder-Adams et al. (2014) with additional
839 resampling from 2014 field season; bentonite ages after Davis et al. (2016). The response to
840 magmatic events is shown through Os_i (94), ^{192}Os and Re curves; the data of these parameters of
841 both field seasons were complementary, but not overlapping. These are plotted against $\delta^{13}C_{org}$
842 and TOC (%) content. Note the marked time interval of the last Strand Fiord volcanic pulse.
843 Elevated Zn/Al and Mn/Al and Fe values point towards hydrothermal activity. Note the different
844 scales in the Zn/Al scale for the 2011 samples (blue) and 2014 samples (black). The iron increase
845 within the Bastion Ridge Formation can be seen on Figure 3C. Age levels are marked by letters,
846 of which A to F are calculated by sedimentation rates according to Davis et al. (2016). The
847 commonly used age levels of A, B and C for the OAE2 interval are adopted here and ages
848 established for the Yezo Group, Japan (duVivier et al., 2015) are listed for comparison.

849 Figure 5: Ratios of TOC (%) over S (%) throughout the section. Note the elevated ratios due to
850 lower concentrations of dissolved sulfate in the brackish to freshwater/terrestrial Bastion Ridge
851 Formation with the exception of the basal interval that delivered benthic foraminifera. Marine
852 values mark the Kanguk Formation.

853 Figure 6: Paleoenvironmental changes over the Cenomanian/Turonian boundary interval at
854 Glacier Fiord. Proxies utilized here include lithology, presence/absence and abundances of
855 benthic foraminifera, their morphotype dominance, $\delta^{13}C_{org}$, TOC (%) content, Hydrogen Index

856 and Os_i variation. In addition, marine (blue) versus brackish/freshwater (grey) intervals are
857 marked.

858

Figure 1
[Click here to download Figure: Figure 1.pdf](#)

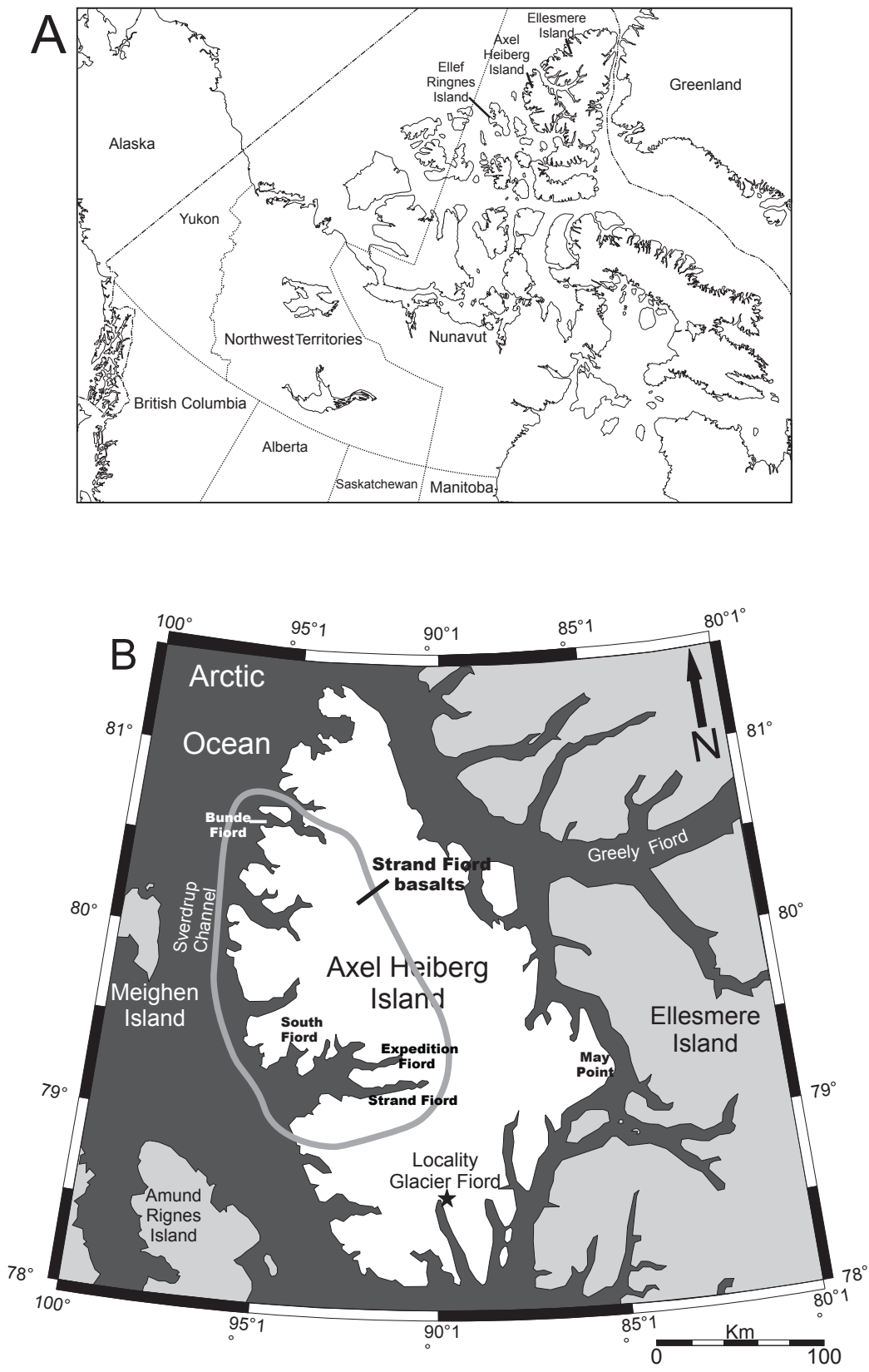


Figure 2

[Click here to download Figure: Figure 2.pdf](#)

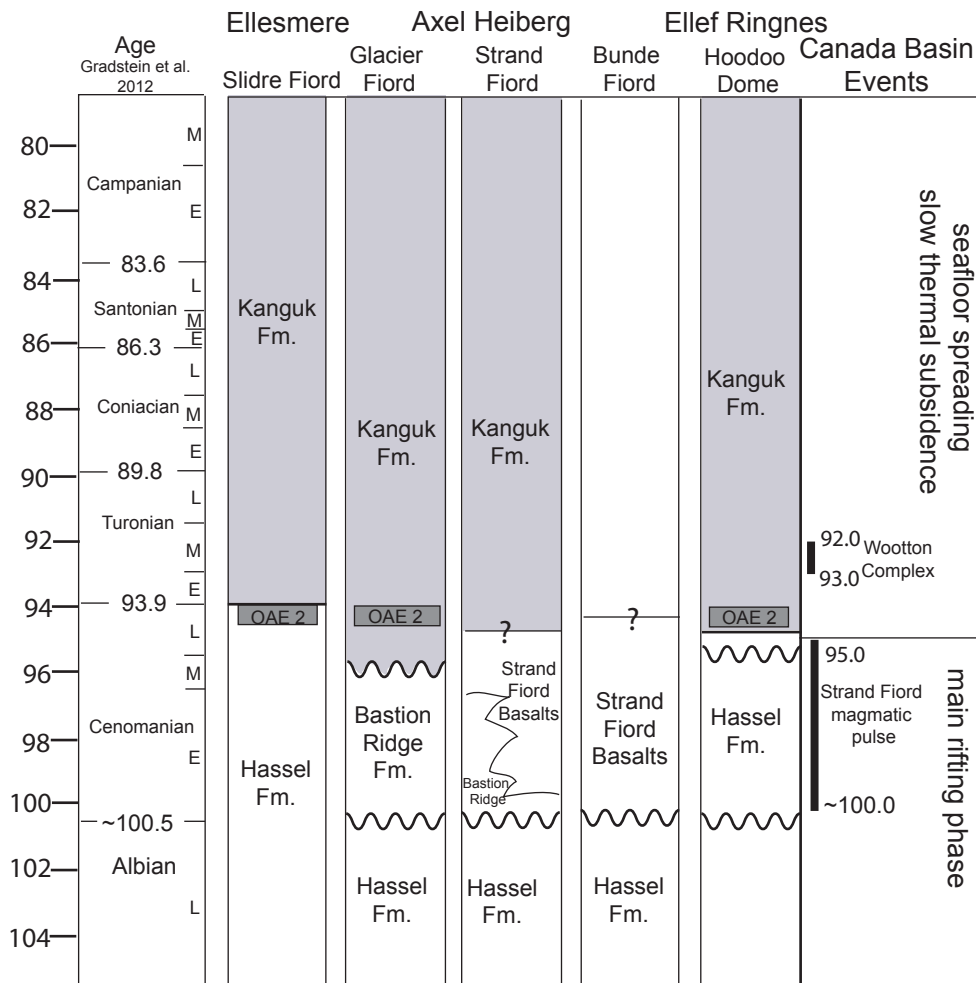


Figure 3
[Click here to download high resolution image](#)

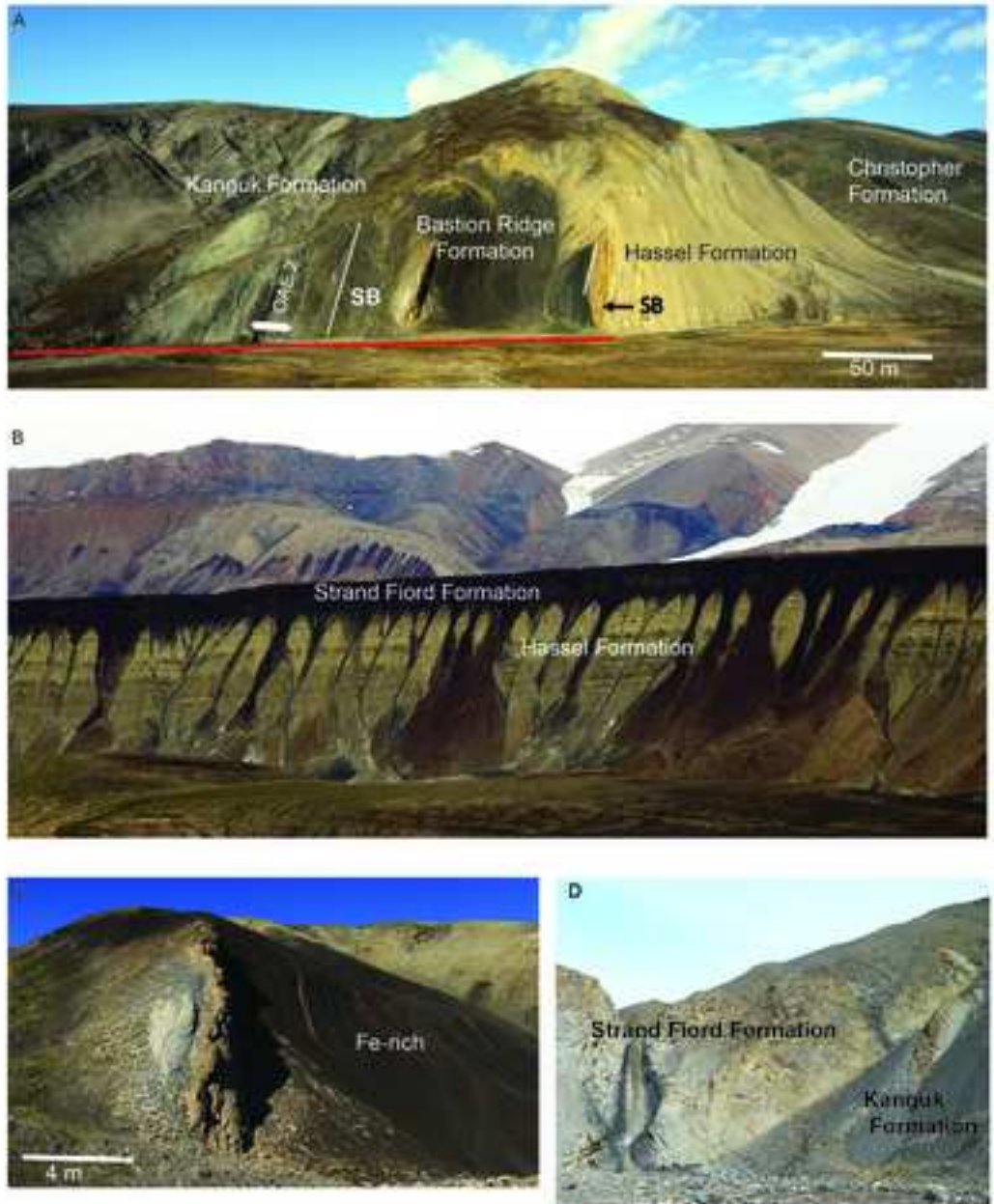


Figure 4
[Click here to download Figure: Figure 4.pdf](#)

Response to Magmatic Events

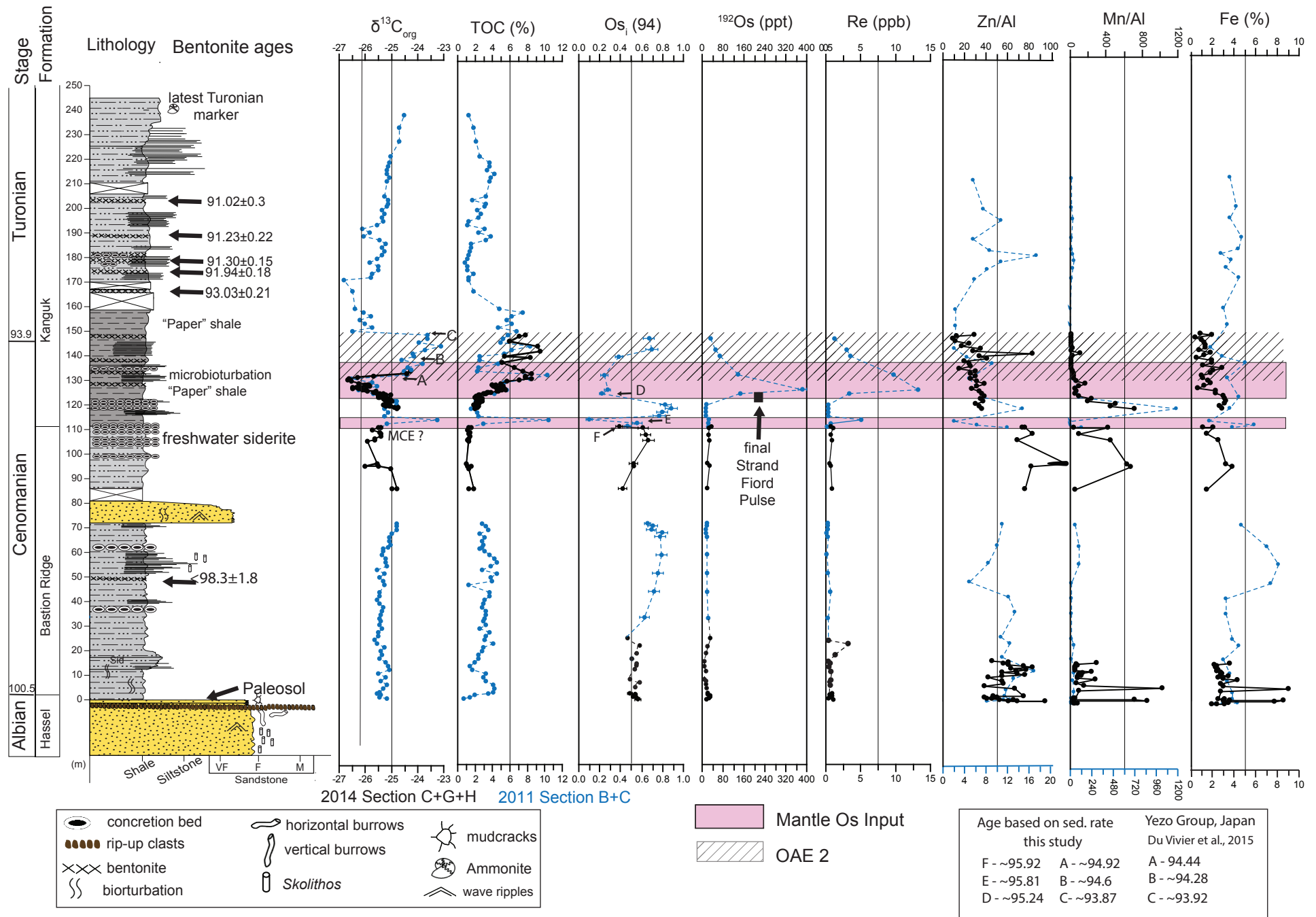
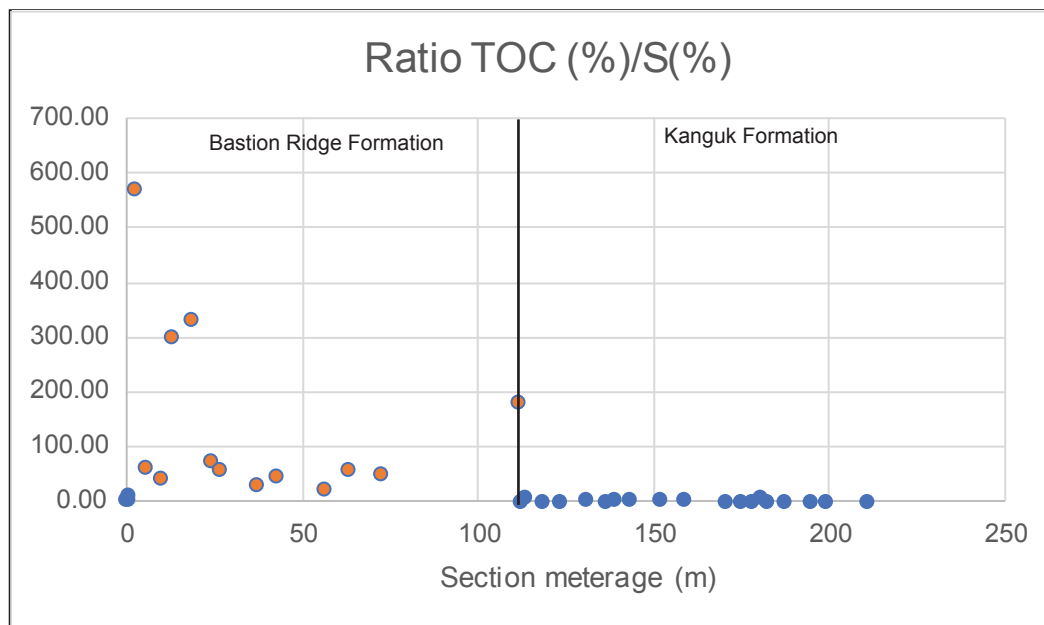


Figure 5

[Click here to download Figure: Figure 5.pdf](#)



Supplementary material for online publication only Methods

[Click here to download Supplementary material for online publication only: Methods for Supplementary Material.docx](#)

Supplementary material for online publication only Table 1

[Click here to download Supplementary material for online publication only: Table 1.xlsx](#)

Supplementary material for online publication only Table 2

[Click here to download Supplementary material for online publication only: Table 2.xlsx](#)

Supplementary material for online publication only Table 3

[Click here to download Supplementary material for online publication only: Table 3.xlsx](#)